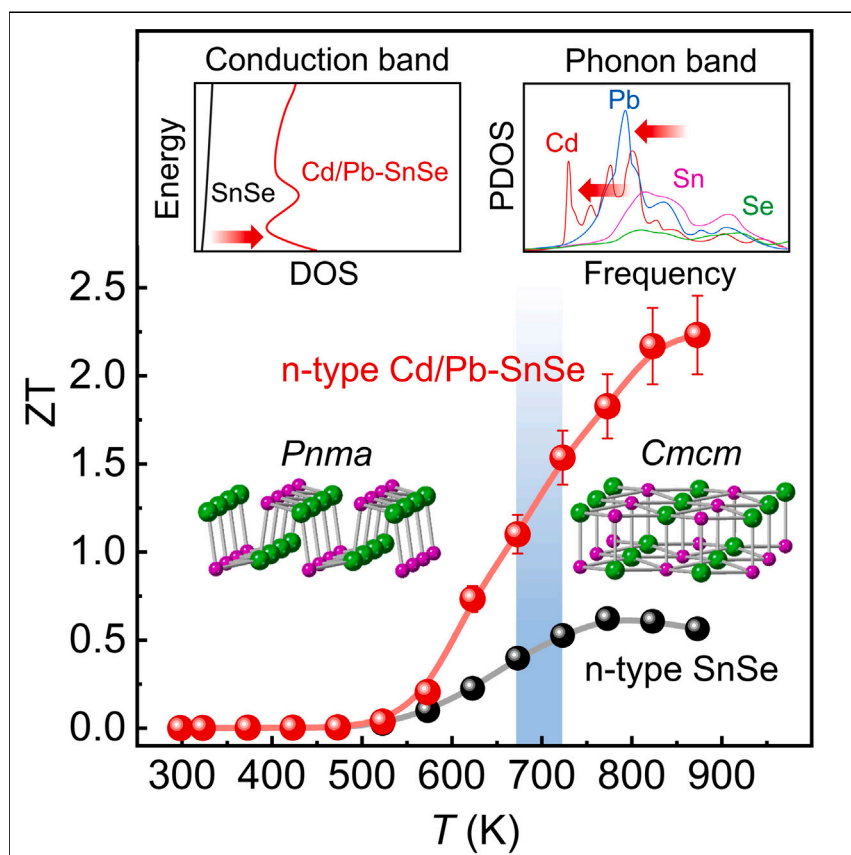 CellPress

Article

Simultaneously engineering electronic and phonon band structures for high-performance n-type polycrystalline SnSe

Sejin Byun, Bangzhi Ge, Hyungjun Song, Sung-Pyo Cho, Moo Sun Hong, Jino Im, In Chung

imjino@krict.re.kr (J.I.)
inchung@snu.ac.kr (I.C.)

Highlights

Cd and Pb favorably manipulate electronic and thermal transport properties of SnSe

Engineering conduction band electronic structures of both *Pnma* and *Cmcm* SnSe phases

Engineering phonon band structures by designing atomic-resolution crystal structure

The ZT ~2.23 is the record-high value for all polycrystalline n-type materials

Our innovative atomic-level crystal lattice engineering, precisely designed by atomic-resolution direct observations, heralds "rational design" of ultrahigh-performance thermoelectric materials. The deliberate introduction of Pb and Cd atoms to SnSe creates unique local crystal structures, according to their coordination chemistry and thermodynamics. These atoms simultaneously manipulate electronic and phonon structures, consequently decoupling and independently controlling physical quantities bound by fundamental physics laws. The achieved thermoelectric figure of merit (ZT) is ~2.23, highest for all n-type polycrystalline materials, surpassing highly expensive PbTe.

Article

Simultaneously engineering electronic and phonon band structures for high-performance n-type polycrystalline SnSe

Sejin Byun,[1] Bangzhi Ge,[2] Hyungjun Song,[1] Sung-Pyo Cho,[3] Moo Sun Hong,[1] Jino Im,[4,*] and In Chung[1,5,*]

SUMMARY

n-type SnSe thermoelectrics has been seriously underdeveloped because of a lack of effective performance-enhancing strategies and doping/alloying agents. Herein, we report that conduction band electronic and phonon structures can be advantageously engineered simultaneously in both *Pnma* and *Cmcm* SnSe phases by dually incorporating Pb and Cd. They enhance the density of states near the conduction band edge in both phases by converging band minima and increasing effective mass (m_0), consequently enhancing Seebeck coefficients (S) without damaging electrical conductivity. Because exclusively divalent Pb and Cd cations reduce innate Sn vacancies, carrier mobility decreases marginally despite the increased m_0 and $|S|$. The tetrahedral Cd displaced from the cationic sublattice and much heavier Pb significantly soften and scatter phonon transport, depressing thermal conductivity significantly. Concurrently improved power factor and decreased thermal conductivity achieve an extraordinarily high thermoelectric (TE) figure of merit, ZT, of ∼2.23 at 873 K, a record high for all polycrystalline n-type TE materials.

INTRODUCTION

The most critical threats facing humanity are the interconnected challenges in energy, climate, and environment. These issues are deeply entwined, with only approximately 30% of the total input being obtained in useable forms of energy, while the remaining 70% is lost as waste heat.[1] The generation of electric energy, primarily reliant on fossil fuels such as coal and natural gas,[1] contributes directly to global warming. Effectively recovering this enormous amount of energy loss holds the key to mitigating these crises. Thermoelectric (TE) technology emerges as a promising solution, providing a means to simultaneously address these global crises.

TE devices, comprising appropriate n- and p-type semiconductors, represent a unique electronic energy converter.[2,3] Operating based on the Seebeck effect, these devices directly transform heat into electric energy without releasing hazardous chemical residues.[4] The performance of TE materials in energy conversion is commonly evaluated using the TE figure of merit, ZT, expressed as $(\sigma S^2)T/\kappa_{tot}$. where σ denotes the electrical conductivity; S represents the Seebeck coefficient; the product σS^2 is the power factor (PF); T denotes the absolute temperature; and κ_{tot} is the total thermal conductivity contributed by charge carriers (electrical thermal conductivity, κ_{ele}) and lattice vibration (lattice thermal conductivity, κ_{lat}).[4] The core factors determining ZT are intricately interconnected by

CONTEXT & SCALE

Thermoelectrics can concurrently address the immediate threats of energy and environmental crises. They generate electricity from huge, ubiquitous, and unavoidable waste heat, thereby reducing consumption of fossil fuels. Improving the thermoelectric (TE) figure of merit (ZT) of n-type materials is a prime task because it seriously restricts ultimate performance of TE devices. Here, a new SnSe-based composition exhibits a record-high ZT of 2.23 reported for all polycrystalline TE systems. Because ZT is a complex combination of electronic and thermal properties, we developed innovative strategies to decouple and independently control them for a higher ZT. The incorporated Cd and Pb atoms generate unique atomic-level local structures, favorably manipulating conduction band electronic and phonon band structures. As a result, enhanced power factor and depressed thermal conductivity yield an exceptionally high ZT in n-type polycrystalline SnSe, far surpassing PbTe and opening a new era of TE technology.

fundamental laws of physics, making it is nearly impossible in principle to independently enhance one desired physical quantity without impacting others adversely.

This presents a formidable challenge in the quest to enhance ZT. Consequently, a prime focus in thermoelectrics has been the development of innovative strategies to decouple these intertwined factors. Representative examples include nanostructuring to suppress κ_{lat},[5] electronic band engineering to achieve higher S without compromising σ,[6] and defect structure engineering to optimize both κ_{lat} and PF simultaneously.[7–11] Notably, recent advancements have introduced a unique enhancement in PF by deviating from the conventional inverse proportionality between charge carrier concentration (n) and mobility (μ). This breakthrough has resulted in an increased σ without detrimentally affecting S.[9,11–13]

PbTe-based materials have been a representative TE system operating in the intermediate- to high-temperature regimes.[14–17] Very recently, PbSe[6–9,11,13,18] and SnSe[19–26] materials have greatly progressed, competing with or even outperforming much more expensive PbTe ones. Particularly, extraordinarily high TE performance has been reported in single-crystal SnSe samples, for example, a ZT of 2.6 at 923 K in p-type pristine crystals along the b axis[19] and 2.8 at 773 K in n-type Br-doped crystals along the a axis.[20] Developing their high-performance polycrystalline versions has thus been a sought-after goal because single crystals are typically unsuitable for mass production and practical TE applications due to the expensive, lengthy, and labor-intensive preparation processes as well as mechanical fragility. Polycrystalline p-type $Na_{0.01}(Sn_{0.95}Pb_{0.05})_{0.99}Se$[21] and $Na_{0.03}Sn_{0.965}Se$[22] eventually exhibit a ZT of ~2.5 at 773 K and ~3.1 at 783 K, respectively, with the solution to the controversial debates on the intrinsic ultralow thermal conductivity of SnSe.[27,28]

However, it has been highly challenging to improve the TE properties of polycrystalline n-type SnSe. Indeed, SnSe is an intrinsic p-type semiconductor because of a substantial degree of inherent Sn vacancies and ubiquitous Sn^{4+} defects. Both effective agents for doping and alloying and performance-enhancing strategies have been seriously elusive. Only four materials show a maximum ZT (ZT_{max}) ≥ ~1.5 to date: $Sn_{0.97}Re_{0.03}Se_{0.93}Cl_{0.02}$ (~1.5 at 793 K)[29]; $Sn_{1.005}Se_{0.94}Br_{0.06}$ (~1.5 at 783 K)[30]; $Sn_{1.08}Se_{0.97}Br_{0.03}−3\%$ PbTe (~1.7 at 793 K)[31]; and $SnSe_{0.92} + 1\%$ $MoCl_5$ (~2.0 at 798 K).[32] Most results mainly focused on reducing κ_{lat}[29,32,33] or enhancing σ.[31,34,35] Enhancing S and PF by modulating electronic band structure has not been reported for n-type polycrystalline SnSe materials.

In striking contrast, for p-type SnSe materials, Na doping has been reported to converge nearby valence-band minima near the Fermi level, consequentially increasing S to give higher PF.[22,36] Engineering electronic band structure is a key strategy to enhance ZT because it can enable the control of interrelated physical quantities such as n, μ, σ, and S independently.

Here, we report a record-high ZT to date for all n-type polycrystalline TE systems in the multielement-alloyed SnSe series, far surpassing the long-standing champion PbTe-based materials. The composition $Cd_x(Sn_{0.76}Pb_{0.24})_{1−x}Se_{0.98}Cl_{0.02}$ (x = 0, 0.0025) innovatively enhances the n-type TE performance of SnSe, a distinct departure from the previous reports. The dually incorporated Pb and Cd atoms play multiple favorable roles in both charge carrier and thermal transport properties of the title materials for TE power generation.

[1]School of Chemical and Biological Engineering, and Institute of Chemical Processes, Seoul National University, Seoul 08826, Republic of Korea

[2]State Key Laboratory of Solidification Processing and Key Laboratory of Radiation Detection Materials and Devices, MIIT, School of Materials Science and Engineering, Northwestern Polytechnical University, Xi'an, Shaanxi 710072, China

[3]National Center for Inter-University Research Facilities, Seoul National University, Seoul 08826, Republic of Korea

[4]Chemical Data-Driven Research Center, Korea Research Institute of Chemical Technology, Daejeon, Republic of Korea

[5]Lead contact

*Correspondence: imjino@krict.re.kr (J.I.), inchung@snu.ac.kr (I.C.)

For electrical transport properties, Pb and Cd atoms first predominantly adopt the divalent formal charge with the Se^{2-} ligand, diverging from Sn. This variance reduces the naturally evolving Sn vacancy, consequently elevating Hall carrier concentration (n_H) to $\sim 10^{19}$ cm^{-3} at high temperatures, resulting in a more than 3.5-fold increase in σ. Second, these atoms favorably manipulate the electronic band structures of both the Pnma and Cmcm phases. Notably, Pb alloying pushes the conduction band minimum (CBM) upward, reducing the energy offset with the overlying second CBM to a negligible value for the Pnma phase. Very importantly, additional Cd incorporation significantly enhances DOS at the conduction band edge by increasing DOS effective mass (m_0) for the Cmcm phase according to our theoretical density functional theory (DFT) calculations.

Consequently, the optimized composition $Cd_{0.0025}(Sn_{0.76}Pb_{0.24})_{0.9975}Se_{0.98}Cl_{0.02}$ can maintain comparably high Seebeck coefficients with the $Sn_{0.76}Pb_{0.24}Se_{0.98}Cl_{0.02}$ without Cd, despite its higher σ. This ultimately improves PF in the high-temperature regime, where SnSe maximally operates as a TE power generator. Despite the significantly heavier m_0, Hall carrier mobility (μ_H) is relatively less damaged, possibly due to the suppressed Sn vacancy by introducing Pb and Cd atoms.

For thermal transport properties, the designed composition strategically places Pb and Cd atoms in the SnSe crystal lattice, aligning with their preferences in coordination chemistry and thermodynamics. Namely, the heavier group 14 congener, Pb, is stabilized in the highly distorted Sn^{2+} cationic sublattice. In contrast, Cd, much smaller and strongly favoring tetrahedral geometry, is displaced from the ideal cationic lattice point. We directly observed their physical locations using an atomic-resolution scanning transmission electron microscope (STEM).

Our theoretical calculations show that the Pb atom softens both acoustic and optical phonon modes through mass fluctuation, and the Cd atom forms a localized band penetrating acoustic phonon modes, inducing resonance scattering and further suppressing κ_{lat}. This atomic-resolution lattice engineering achieves ultralow κ_{tot} without deteriorating PF. Remarkably, the κ_{lat} of the $Cd_{0.0025}(Sn_{0.76}Pb_{0.24})_{0.9975}Se_{0.98}Cl_{0.02}$ sample decreases continuously across the phase transition regime from 0.40 W m^{-1} K^{-1} at 300 K to 0.24 W m^{-1} K^{-1} at 873 K.

The concurrent enhancement of PF and depression of κ_{tot} boosts a ZT_{max} of the $Cd_{0.0025}(Sn_{0.76}Pb_{0.24})_{0.9975}Se_{0.98}Cl_{0.02}$ sample reaching ~ 2.23 at 873 K, outperforming all n-type polycrystalline TE systems such as PbTe (~ 1.9 for $Pb_{0.98}Sb_{0.02}Te$)[37]; PbSe (~ 1.8 for $PbSe_{0.998}Br_{0.002}$–2% Cu_2Se)[8]; $SnSe_{0.92}$ + 1% $MoCl_5$ (~ 2.0 at 798 K)[32]; and $AgPb_mSbTe_{2+m}$ (~ 2.2 for $AgPb_{18}SbTe_{20}$).[14]

RESULTS AND DISCUSSION

Design principle and crystal structure

SnSe crystallizes in orthorhombic GeS-type structure, featuring corrugated two-atom-thick SnSe layers. Above the onset temperature (T_c) of ~ 777 K,[38] it undergoes a characteristic reversible phase transition from the Pnma to the higher symmetry Cmcm space group (Figure 1A). The Sn^{2+} coordination center with active $5s^2$ lone pair electrons creates a highly anisotropic coordination environment, resulting in a severely distorted $[SnSe_7]$ polyhedron with distinct three short (2.7–2.8 Å) and four long Sn–Se bonds (3.3–4.1 Å).[39] This unique structural feature generates intrinsic electronic and phonon structures that are highly advantageous for TE performance.
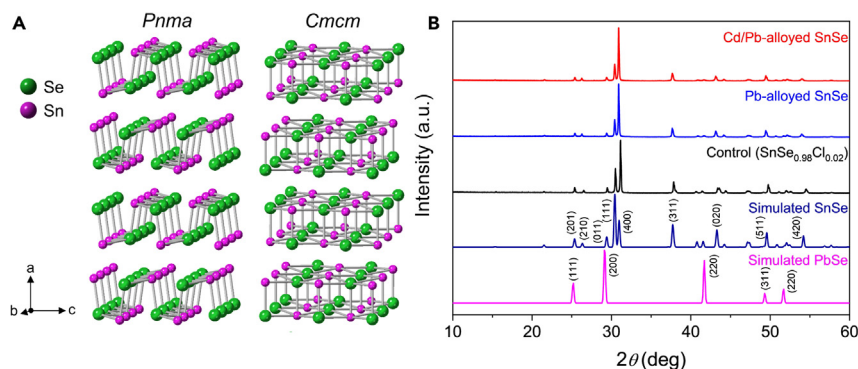
Figure 1. Crystal structures and PXRD patterns

(A) Crystal structures of SnSe with *Pnma* and *Cmcm* space groups displaying highly anisotropic layered structure.

(B) PXRD patterns of the $SnSe_{0.98}Cl_{0.02}$ (control), $Sn_{0.76}Pb_{0.24}Se_{0.98}Cl_{0.02}$ (Pb-alloyed SnSe), and $Cd_{0.0025}(Sn_{0.76}Pb_{0.24})_{0.9975}Se_{0.98}Cl_{0.02}$ (Cd/Pb-alloyed SnSe) samples in comparison with the theoretical simulation for *Pnma* SnSe (The International Centre for Diffraction Data [ICDD] PDF 48−1224) and PbSe (PDF 06−0354). Major Bragg peaks are indexed.

Concurrently, while advantageous for TE performance, the SnSe structure may limit effective doping and alloying to the cationic sublattice, making it challenging to manipulate the electronic structure and to expand compositional variance in SnSe thermoelectrics. For example, attempts to modify the composition $SnSe_{0.92}$ with 1 mol % $MoCl_5$ leads to the formation of an intergrown modular nanostructure of $[(SnSe)_{1.05}]_m[MoSe_2]_n$ rather than altering the electronic structure by placing Mo atoms at the Sn site.[32] The Re atom shows a low solubility in the SnSe matrix, thereby being isolated as nanoscale precipitates.[29]

A naturally evolving Sn vacancy induces intrinsic p-type conduction with a low hole carrier concentration of $\sim 10^{17}$ cm^{-3} near room temperature. The presence of Sn^{4+} frequently restricts reliable n-type conduction by doping cations with a higher formal charge, for example, Sb^{3+} and Bi^{3+}.[40,41] As a result, it is difficult to stabilize an electron-doped state in SnSe over a wide range of temperature. Halogen atoms are a typical electron dopant for n-type SnSe as reported in $SnSe_{1-x}Cl_x$ ($x \geq 0.02$)[29,33] in which Cl doping pushes the Fermi level into the conduction band edge.

To develop a new high-performance n-type SnSe system, preliminary investigations involved Pb alloying up to 24 mol % to the $SnSe_{0.98}Cl_{0.02}$ matrix. We expected that it can simultaneously contribute to suppressing thermal transport and improving charge carrier transport. Pb, as a heavier group 14 congener, generates point defects and induces considerable mass fluctuation, effectively scattering heat-carrying phonons and decreasing thermal conductivity. It also adopts a divalent formal charge with chalcogenide ligands (S^{2-}, Se^{2-}, and Te^{2-}), contributing to enhancing n-type conduction by decreasing vacancies at the cationic sublattice (V_{cation}).[42]

Indeed, our $Sn_{1-x}Pb_xSe_{0.98}Cl_{0.02}$ ($x = 0–0.24$) system demonstrates an increase in electrical conductivity (σ) and a decrease in total thermal conductivity (κ_{tot}) as x increments up to 0.24, preserving SnSe crystal structure (Figures 2 and S1). Resultantly, the $x = 0.24$ sample exhibits a highest ZT of ~ 1.7 at 873 K among the series parallel to the pressing direction of spark plasma sintering (SPS).

We further incorporated Cd atom into the best-performing composition of $Sn_{0.76}Pb_{0.24}Se_{0.98}Cl_{0.02}$ (Pb-alloyed SnSe), and obtained the $Cd_{0.0025}$
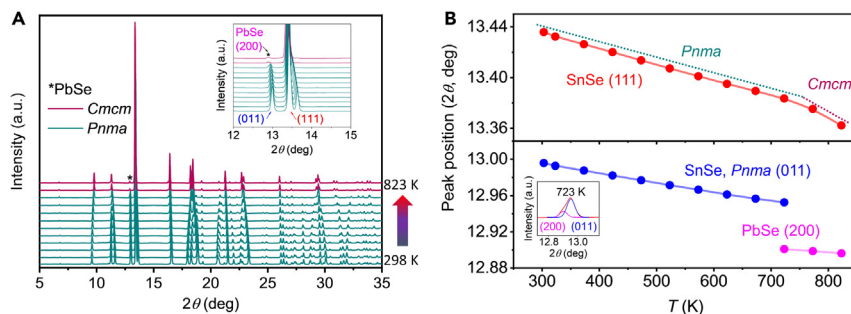
Figure 2. *In situ* temperature-dependent SR-XRD patterns

(A) *In situ* temperature-dependent SR-XRD patterns for the Cd/Pb-alloyed SnSe sample from 298 to 823 K with the interval of 50 K. The inset focuses on the characteristic (011) peak of *Pnma* SnSe phase. Its disappearance indicates the critical phase transition from *Pnma* to *Cmcm* space group. (B) The shift in the (011) and (111) reflections for SnSe and the (200) reflection for PbSe upon heating. Inset: the deconvolution of the signal around 12.9° at 723 K, revealing the (011) and (200) reflection peaks for *Pnma* SnSe and PbSe, respectively.

$(Sn_{0.76}Pb_{0.24})_{0.9975}Se_{0.98}Cl_{0.02}$ (Cd/Pb-alloyed SnSe) sample. The Cd atom, preferring divalent formal charge and tetrahedral coordination with chalcogenide ligands, is possibly incompatible to the highly distorted Sn^{2+} coordination center with a $5s^2$ electron lone pair. If displaced from the Sn^{2+} cationic sublattice, it may induce a substantial reduction in κ_{tot} through phonon softening[8,43] and scattering in the low frequency regime.[44,45] Our discussion will primarily focus on the title Pb-alloyed SnSe and Cd/Pb-alloyed SnSe samples in comparison with the control $SnSe_{0.98}Cl_{0.02}$ composition.

All samples appear to form a pure phase at room temperature, well within the detection limit of laboratory powder X-ray diffraction (PXRD) data, matching precisely the *Pnma* SnSe structure (Figure 1B). The refined cell dimensions are given in Table S1. The experimentally determined band gap is ~0.93 eV for all samples at room temperature (Figure S3).

Given the prior observation that alloying with Pb gradually reduces the T_c of SnSe,[38] we conducted an in-depth investigation into the crystal structure of the Cd/Pb-alloyed SnSe sample from room temperature to 823 K, utilizing *in situ* temperature-dependent synchrotron radiation XRD (SR-XRD) (Figure 2A). A continuous structural transformation is evident between 673 and above 723 K, consistent with the onset T_c observed at 678 K according to our differential scanning calorimetry (DSC) result (Figure S4).

The main signal for both *Pnma* and *Cmcm* phases is the (111) Bragg reflection around 13.4°, which exhibits a nearly linear downshift upon heating from 300 to 723 K. Subsequently, the shift becomes more pronounced, signaling a symmetry change from the *Pnma* to *Cmcm* space group (Figure 2B). The characteristic (011) reflection around 12.9° of the *Pnma* phase also undergoes a nearly linear downward shift in 2θ from 300 to 723 K, with its intensity gradually decreasing between 673 and 723 K (Figures 2B and S5). At 723 K, the (011) reflection curve splits, revealing a concealed signal corresponding to the (200) reflection of PbSe (Figure 2B, inset). Beyond 773 K, the (011) peak of the *Pnma* phase ultimately disappears. This observation shows that the Cd/Pb-alloyed SnSe sample undergoes continuous phase transition between 673 and 773 K, a range significantly lower than the ~750–800 K observed for pristine SnSe.[19] This result underscores the efficacy of alloying as a

means to tune the T_c of SnSe for enhanced TE performance within a desired temperature regime.

The (200) reflection of PbSe becomes evident at 12.9° above 773 K in the temperature regime of the *Cmcm* phase, as it overlaps with the strong (011) reflection of the *Pnma* phase (Figures 2A and S5). Indeed, micrometer-sized PbSe precipitates are observed embedded in the surround matrix in our scanning electron microscopy observation (Figure S6). Therefore, thorough structural inspections are imperative for high concentration Pb-alloyed SnSe samples. *In situ* temperature-dependent SR-XRD patterns, DSC, thermogravimetric analysis (TGA), and PXRD patterns conducted before and after TE property measurements (Figures S4, S7, and S8) confirm that PbSe neither decomposes nor reacts with the surrounding matrix throughout the entire temperature range. Consequently, the presence of PbSe does not compromise the repeatability of the TE performance of the investigated materials.

Local structures

We investigated atomic-resolution local structures of the Cd/Pb-alloyed SnSe sample using a spherical aberration-corrected STEM (Cs-corrected STEM) equipped with an energy-dispersive X-ray spectroscopy (EDS) and electron-energy-loss spectroscopy (EELS) detectors. It is of prime importance in determining the precise physical location of incorporated Cd and Pb atoms within the highly distorted SnSe lattice by direct observation given the distinct coordination chemistry of Cd compared with Pb and Sn atoms. The resulting local defect structures can interact uniquely with charge carriers and heat-carrying phonons, significantly influencing their TE properties. Consequentially, gaining insights into the behavior of specific atoms within a given crystal lattice at the atomic level, particularly atomic-level coordination chemistry, is imperative for rational "design" of high-performance TE materials.

All STEM images were captured down the [010] zone axis, aligning with the linear arrangement of respective Sn and Se atoms (Figure 3). This alignment facilitates the clear distinction of each atom through the combination of STEM, EDS, and EELS results. Typical low-magnification high annular angle dark field (HAADF)-STEM imaging shows the presence of nanoscale local structures randomly distributed in the matrix (Figure 3A). The corresponding electron diffraction pattern in Figure 3A perfectly matches with the *Pnma* SnSe structure along the [010] zone axis with no evidence of secondary phases or satellite peaks (Figure 3A, inset). This indicates that the nanoscale local structures form coherent interfaces with the SnSe matrix. This observation implies that they serve as efficient phonon scattering mechanisms and have a minimal impact on the deterioration of charge carrier transport.

A typical HAADF-STEM image taken in a defect-free region reveals the characteristic atomic arrangement of the *Pnma* SnSe structure (Figure 3B). In the magnified HAADF-STEM, a noticeable distinction emerges between larger, brighter spheres and smaller, fainter counterparts (Figure 3C). The former can tentatively be attributed to the heavier cationic sublattice containing ^{50}Sn and ^{82}Pb, while the latter corresponds to lighter ^{34}Se anionic sublattice. This assignment is based on their respective HAADF signal intensities, which exhibit a rough proportionality to the square of their atomic numbers. The elemental distribution map directly scanned on Figure 3C by STEM-EDS confirms the aforementioned atomic arrangement (Figure 3D). The Sn (pink) and Pb (yellow) atoms are randomly distributed within the cationic sublattice. Notably, there are no observed satellite or displaced atoms in this area.
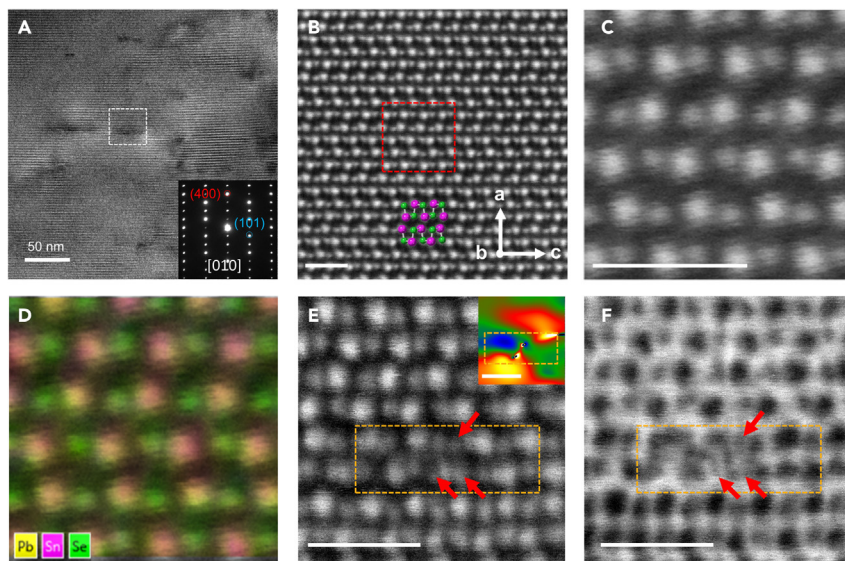
Figure 3. Cross-sectional STEM images and elemental mapping for the Cd/Pb-alloyed SnSe sample down the [010] zone axis

(A) A typical low-magnification HAADF-STEM image showing the presence of nanoscale defects. Inset: the corresponding selected area electron diffraction pattern, aligning precisely with the *Pnma* SnSe structure viewed down the [010] zone axis.

(B) The HAADF-STEM image taken on the defect-free region in (A).

(C) The magnified atomic-resolution HAADF-STEM image taken on the red rectangle in (B).

(D) The atomic-resolution elemental mapping by STEM-EDS scanned on the entire area in (C), clearly revealing the randomly distributed Sn and Pb atoms at the cationic sublattice.

(E) HAADF-STEM images taken on the white square in (A) displaying the presence of satellite atoms (red arrows) and consequent significant lattice distortion in the orange rectangle. Inset: GPA image of (E) along the y axis (ε_{yy}) showing accumulated strains around the distorted lattice.

(F) The corresponding ABF STEM image of (E). Scale bars in (B–F) are 1 nm.

The magnified HAADF-STEM image, captured at the nanostructure enclosed by the white broken line in Figure 2A, displays a distorted SnSe lattice (orange broken line) with weak satellite signals (red arrows) near the Sn atoms (Figure 3E). A strain map profile (ε_{yy}) for Figure 3E was derived by geometric phase analysis (GPA), a semi-quantitative process for high-quality TEM images to obtain spatially distributed strain fields (inset). This result verifies that high strain concentrations along the *a* axis near the distorted SnSe lattice. These strains are likely induced primarily by the presence of displaced Cd atoms causing distortion in the atomic arrangement of the Sn/Pb and Se atoms.

The corresponding annular bright-field (ABF) STEM image more clearly depicts the presence of the introduced light atoms, severely distorting the atomic arrangement around them (Figure 3F). The satellite atom is unambiguously identified as the alloyed Cd atom showing the Cd $M_{4,5}$ edge at 404 eV, discernible from the Sn $M_{4,5}$ edge at 485 eV in the EELS spectrum obtained by a STEM-EELS elemental scan profile (Figure S9). This direct observation of the defect structure is consistent with coordination chemistry expected from the Cd atom, which strongly prefers tetrahedral geometry and thus is incompatible with the highly anisotropic Sn^{2+} cationic sublattice.

The resulting local structure modulation can significantly increase bonding anharmonicity, serving as a highly effective phonon scattering mechanism. Similar

observations have been reported in other materials such as rock-salt structure PbSe alloyed with Cd[44] and Hg.[6] Importantly, isolated CdSe precipitates are not observed, which is crucial for overall TE performance of the material, given the much higher thermal conductivity of bulk CdSe[46] of $\sim$9 W m^{-1} K^{-1} compared with SnSe.

Charge transport properties

SnSe adopts the characteristic lamellar structure, thereby exhibiting highly anisotropic charge carrier and thermal transport properties according to the pressing directions of consolidation of polycrystalline powders.[21,22] Our discussion will primarily focus on TE properties parallel to the pressing direction of SPS because of a higher ZT along this direction, unless noted otherwise.

The results of temperature-variant Hall effect measurement provide important understanding for effects of Pb and Cd incorporation to the SnSe lattice on charge transport properties. Initially, all samples show very low Hall carrier concentration (n_H) prior to the thermal activation of charge carriers at elevated temperatures. Intrinsic p-type, undoped polycrystalline SnSe, for instance, presents n_H of $\sim$10^{17} cm^{-3} at 300 K.[38] The n_H of the heavily alloyed title samples remains at an order of $\sim$10^{17}–10^{18} cm^{-3}. In contrast, the control sample experiences an increase from an order of $\sim$10^{15} to $\sim$10^{17} cm^{-3} in the temperature range of 300–473 K (Figure S10A). The remarkably low n_H at low temperatures, in contrast to that of single-crystal SnSe samples, can be attributed to the presence of ubiquitous Sn^{4+} and vacancies at grain boundaries in polycrystalline samples. As the temperature rises, the n_H undergoes a rapid increase. At 673 K, it reaches 3.8 × 10^{18}, 1.2 × 10^{19}, and 1.7 × 10^{19} cm^{-3} for the control, Pb-alloyed, and Cd/Pb-alloyed SnSe samples, respectively.

The Hall carrier mobility (μ_H) of all samples increases from 300 to 473 K, despite the trend observed in their respective n_H (Figure S10B). This phenomenon can be attributed to barrier-like scattering arising from defects or impurities at grain boundaries.[47] Subsequently, μ_H decreases up to $\sim$573 K as n_H increases rapidly, and then continuously increases. This observation can be understood by the change in the energy offset (ΔE) between the minimum of the first and second conduction bands of SnSe, where the ΔE gradually decreases and then increases with rising temperature.[20] Consequently, the μ_H of n-type SnSe increases considerably at high temperature as observed in the previous reports on n-type SnSe materials.[20,42] In the title samples, the effect of decreasing ΔE on μ_H at lower temperatures is mitigated by the abrupt rise in n_H.

Notably, Pb alloying simultaneously increases n_H and μ_H in contrast to their general inverse proportionality. This effect is attributed to the filling of naturally evolving, adverse Sn vacancies, which act as a source of hole carriers and strong vacancy scattering centers. The introduction of Cd to the Pb-alloyed SnSe sample further reduces Sn vacancies, increasing n_H. However, it induces local distortions, slightly decrementing μ_H. Consequently, determining the concentration of Pb and Cd in SnSe is crucial to optimize both n_H and μ_H to achieve maximal charge transport properties.

The electrical conductivity (σ) of the title samples shows nearly negligible temperature dependence with a very low value of $\sim$1 S cm^{-1} up to $\sim$473 K primarily due to a low n_H (Figure 4A). In comparison, the σ of the control sample initiates a rise at the lower temperature of $\sim$373 K, reaching 0.25 S cm^{-1} at $\sim$473 K. Subsequently, their σ abruptly rises with increasing temperature due to improved n_H resulting
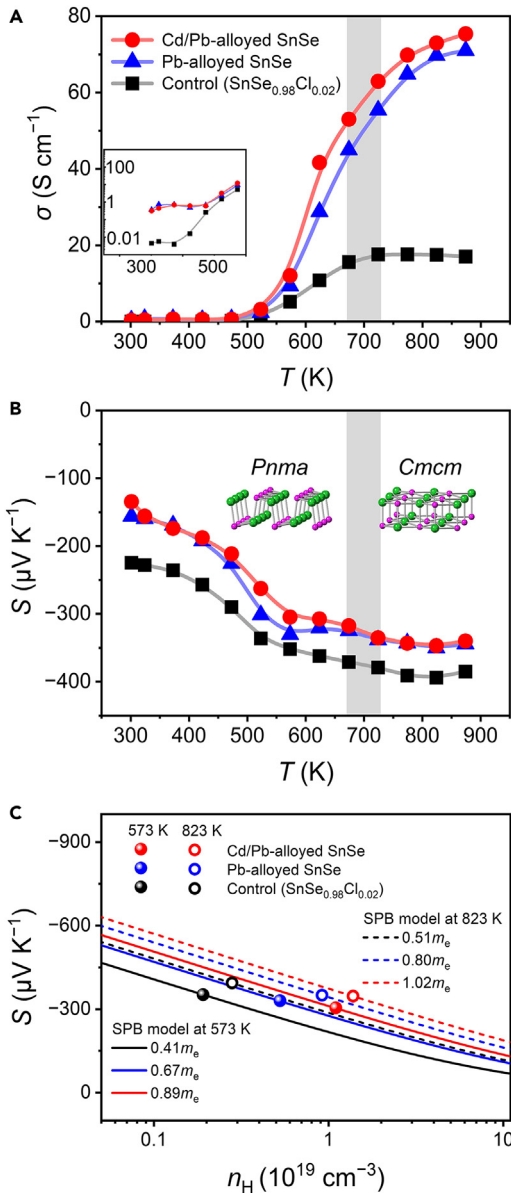
Figure 4. Charge carrier transport properties

(A and B) Temperature-dependent (A) electrical conductivity (σ) and (B) Seebeck coefficient (S) parallel to the SPS pressing direction for the control, Pb-alloyed SnSe, and Cd/Pb-alloyed SnSe samples. The continuous $Pnma$-$Cmcm$ phase transition region between 673 and 723 K for the Cd/Pb-alloyed SnSe sample is presented in gray.

(C) The theoretical Pisarenko plots based on a single parabolic band (SPB) model for the control sample ($SnSe_{0.98}Cl_{0.02}$) with the density of states effective mass (m_0) of $0.41m_e$ at 573 K ($Pnma$ phase, black solid line) and $0.51m_e$ at 823 K ($Cmcm$ phase, black dashed line). Experimental Seebeck coefficients of the Pb-alloyed SnSe and Cd/Pb-alloyed SnSe samples (blue and red symbols) lies far above the theoretical Pisarenko line at a given n_H at 573 and 823 K. A nonlinear fit of a SPB model represent the corrected m_0 of the title samples: $m_0 = 0.67m_e$ at 573 K (blue solid line) and $m_0 = 0.80m_e$ at 823 K (blue dashed line) for Pb-alloyed sample; and $m_0 = 0.89m_e$ at 573 K (red solid line) and $m_0 = 1.02m_e$ at 823 K (red dashed line) for the Cd/Pb-alloyed sample.

from thermal activation. Pb alloying markedly improves σ over the entire range of temperature because of the unusual simultaneous increase in n_H and μ_H given the relation $\sigma = e \cdot n_H \cdot \mu_H$. Specifically, the σ of the control, Pb-alloyed SnSe, and Cd/Pb-alloyed SnSe samples is 0.004, 0.368, 0.318 S cm^{-1} at 300 K and 17.07, 71.01, 75.37 S cm^{-1} at 873 K, respectively. The σ values of the title samples above 773 K surpass those of the previously reported state-of-the-art n-type polycrystalline SnSe materials.[29–32] For example, $Sn_{0.97}Re_{0.03}Se_{0.93}Cl_{0.02}$[29]; $Sn_{1.005}Se_{0.94}Br_{0.06}$[30]; $Sn_{1.08}Se_{0.97}Br_{0.03}$–13% PbTe[31]; and $SnSe_{0.92}$ + 1% MoCl$_5$[32] show ~32 S cm^{-1} at 798 K, ~32 S cm^{-1} at 783 K, ~60 S cm^{-1} at 793 K, and ~41 S cm^{-1} at 827 K, respectively. Note that σ of the title sample continuously increases across the temperature regime of the $Pnma$-$Cmcm$ structural phase transition.

Importantly, the temperature-dependent Seebeck coefficient (S) values reveal the impact of alloying Pb and Cd atoms on the electronic structures of the samples. Across the entire temperature range of measurements, all samples consistently exhibit a negative sign of S, which is indicative of their stable n-type conduction (Figure 4B). The title samples show a smaller magnitude of S ($|S|$) values than the control sample because of their significantly higher n_H, which is in line with the direct proportionality of $|S|$ to the product of $n_H^{-2/3}$ and DOS effective mass (m_0). However, the discrepancy in their $|S|$ is not as significant as that in their σ given the general inverse proportionality between $|S|$ and σ. Remarkably, the Cd/Pb-alloyed SnSe sample shows a comparable $|S|$ with the Pb-alloyed SnSe sample, despite its higher n_H and σ. Hence, their intrinsic physical relations are favorably broken to achieve higher TE performance. These observations indicate that both Pb and Cd atoms alloyed to the Cl-doped SnSe lattice advantageously modulate conduction band electronic structure to enhance charge transport properties.

To delve into the effects of incorporating Pb and Cd on S, the Pisarenko relation between S and n_H for SnSe$_{0.98}$Cl$_{0.02}$ with a $m_0 = 0.41m_e$ at 573 K (*Pnma* phase, black solid line) and a $m_0 = 0.51m_e$ at 823 K (*Cmcm* phase, black dashed line) are theoretically plotted based on a single parabolic band (SPB) model assuming acoustic phonon interaction as a dominant scattering mechanism (Figure 4C) (see supplemental information for details). The control sample shows the $|S|$ values falling well on the Pisarenko lines at both temperatures. In striking contrast, the Pb-alloyed SnSe and Cd/Pb-alloyed SnSe samples deviate significantly above these lines, indicating a significant departure from the expected behavior. A nonlinear fit of the SPB model yields the corrected m_0 of the title samples: $m_0 = 0.67m_e$ at 573 K (blue solid line) and $m_0 = 0.80m_e$ at 823 K (blue dashed line) for the former; and $m_0 = 0.89m_e$ at 573 K (red solid line) and $m_0 = 1.02m_e$ at 823 K (red dashed line) for the latter, highlighting their advantageous modulation of conduction band electronic structure to enhance charge transport properties.

It is important to note that the band edges of the first and second conduction bands of SnSe naturally converge gradually on heating until ~600 K, diverging afterward.[20] However, this advantageous effect is not reflected in the control sample at 573 K, indicating a need for effective strategies to enhance $|S|$ in the high-temperature regime, particularly the postphase transition to the *Cmcm* phase. Given the largely increased m_0, Pb alloying significantly manipulates conduction bands near the Fermi level for both the *Pnma* and *Cmcm* phases and increases $|S|$ far beyond the theoretical expectations. Remarkably, additional Cd alloying to the Pb-alloyed SnSe sample even further improves $|S|$ at a given n_H while maintaining the higher σ. Consequently, higher $|S|$ values of the title samples could arise from additional favorable mechanisms.

Electronic band structures

To comprehend the effects of alloying Pb and Cd on charge transport properties, particularly the unusually enhanced $|S|$ and m_0, we performed electronic structure calculations for the title and control samples for both the low-temperature *Pnma* and high-temperature *Cmcm* phases within the DFT formalism (Figure 5). The representation of the title composition involved Pb atoms randomly replacing Sn atoms at the cationic sublattice, and Cd atoms located off-centered from it with an additional Sn vacancy. This gave a $2\sqrt{2} \times 2\sqrt{2} \times 1$ supercell of "Sn$_{24}$Pb$_8$Se$_{32}$" and "Cd$_1$Sn$_{24}$Pb$_7$Se$_{32}$" accommodating 64 atoms. Because of the cell-size limitation in computation, a larger degree of Cd alloying was considered than the experimental compositions.
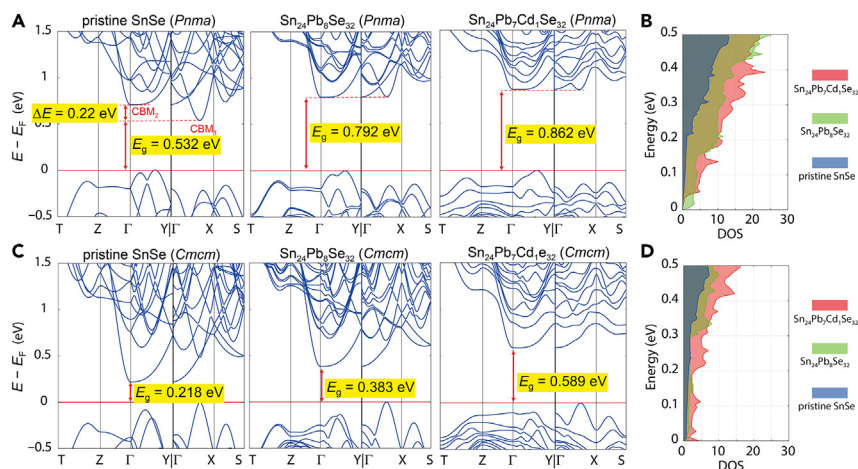
Figure 5. Electronic band structures

(A) Calculated electronic band structures of pristine SnSe (left), Pb-alloyed SnSe (center), and Cd/Pb-alloyed SnSe (right) of *Pnma* phase.

(B) DOS of three compounds of *Pnma* phase. CBMs set to zero energy level.

(C) Calculated electronic band structures of pristine SnSe (left), Pb-alloyed SnSe (center), and Cd/Pb-alloyed SnSe (right) of *Cmcm* phase.

(D) DOS of three compounds of *Cmcm* phases. The CBMs are set to a zero energy level. The conduction band minima (CBM1 and CBM2), energy offset (ΔE), and band gap (E_g) are given.

In the *Pnma* phase, pristine SnSe presents multibands near the CBM energy level (Figure 5A). The lowest energy CBM1 with the light calculated m_0 of $0.09m_e$ emerges between the Γ and X points. The second lowest energy CBM2 is located at the Γ point. The corresponding band is significantly anisotropic, consequently giving a m_0 of $0.921m_e$, $155.5m_e$, and $0.065m_e$ along the Γ-X, Γ-Y, and Γ-Z, respectively. The energy offset between the CBM1 and CBM2 ($\Delta E_{CBM2\text{-}CBM1}$) is 0.22 eV. Notably, the high concentration Pb alloying shifts the CBM1 up, converging the two adjacent band minima to give the negligible $\Delta E_{CBM1\text{-}CBM2}$, increasing the band gap (E_g) from 0.532 to 0.792 eV, and enhancing the DOS at the band minima (Figure 5B). Consequently, $|S|$ increases without deteriorating σ, consistent with our experimental observations. No noticeable change in a m_0 is observed for both the light and heavy bands. However, dispersion of the heavy band along the Γ-Y slightly deforms, giving a smaller effective mass of $38.3m_e$.

The Cd incorporation to the *Pnma* Pb-alloyed SnSe phase further enlarges the band gap, but mainly preserves the band convergence feature driven by Pb alloying except for slight changes at the CBMs (Figure 5A). Specifically, the E_g increases from 0.792 to 0.862 eV, and the light band between the Γ and X points slightly moves toward a lower energy level.

The *Cmcm* phase generates very different conduction band minima compared with the *Pnma* phase (Figure 5C). Pristine SnSe displays only a single anisotropic band at the Γ point near the CBM. The high concentration Pb alloying increases the m_0 from $0.76m_e$ to $0.87m_e$, from $2.21m_e$ to $5.45m_e$, and from $0.072m_e$ to $0.075m_e$ along the Γ-X, Γ-Y, and Γ-Z, respectively.

The Cd incorporation to the *Cmcm* Pb-alloyed SnSe phase also enlarges the band gap from 0.383 to 0.589 eV. As a result, the band edge becomes more flattened, which can contribute to increasing $|S|$. The manipulated CBMs by alloying Pb and Cd atoms are evident in the DOS plots of the title and control *Cmcm* phases
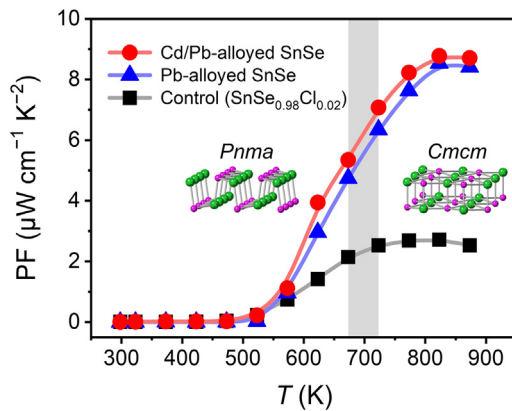
Figure 6. Power factor

The temperature-dependent power factor (PF) parallel to the SPS pressing direction for the control, Pb-alloyed SnSe, and Cd/Pb-alloyed SnSe samples. The continuous *Pnma-Cmcm* phase transition region between 673 and 723 K for the Cd/Pb-alloyed SnSe sample is presented in gray.

(Figure 5D). As Pb and Cd atoms are sequentially incorporated to the SnSe, the DOS of the CBMs are gradually enhanced. The induced enhancement in the DOS near the Fermi level and effects of CBM convergence clearly explain the experimentally observed enhancement in $|S|$ in the title samples. Remarkably, alloying Pb and Cd atoms concurrently manipulate both the *Pnma* and *Cmcm* phases favorably, consistent with our experimental observations. Note that a loss in μ_H is only marginal despite the much heavier m_0 in the title samples. This unusual observation can be attributed to the alloyed Pb and Cd occupying intrinsic and unfavorable Sn vacancies for n-type TE performance.

Power factor

The heavily alloyed Pb atoms enhance n_H and μ_H simultaneously across the entire temperature range. Both the Pb and Cd incorporations increase m_0 by the effect of band convergence in the *Pnma* phase and band flattening in the *Cmcm* phase, thereby improving $|S|$ without causing damage to σ. Note that they reduce Sn vacancy scattering centers when introduced into the SnSe matrix, improving m_0 at the conduction band edge without significant damage for the μ_H. The synergistic effect of unusually improved charge transport properties results in the greatly improved PF for the Pb-alloyed samples (Figure 6). Note that the unusual simultaneous increase in σ and $|S|$ with higher temperatures results in a maximum PF (PF_{max}) in the high-temperature region. The Cd/Pb-alloyed SnSe sample shows a PF_{max} of $\sim$ 8.8 $\mu W\ cm^{-1}\ K^{-2}$ at 823 K along parallel to the SPS direction, surpassing that of the control sample by $\sim$300%. In comparison, the PF_{max} of the state-of-the-art n-type polycrystalline SnSe materials along the same direction is $\sim$6.0, 6.8, 8.3, and 8.7 $\mu W\ cm^{-1}\ K^{-2}$ for $Sn_{0.97}Re_{0.03}Se_{0.93}Cl_{0.02}$,[29] $Sn_{1.005}Se_{0.94}Br_{0.06}$,[30] $Sn_{1.08}Se_{0.97}Br_{0.03}$—13% PbTe,[31] and $SnSe_{0.92}$ + 1% $MoCl_5$,[32] respectively.

Thermal transport properties

The Pb alloying substantially decreases total thermal conductivity (κ_{tot}) in the low to medium temperature range from 300 to 573 K of the title samples. Specifically, the κ_{tot} of the control; Pb-alloyed SnSe; and Cd/Pb-alloyed SnSe is 0.67, 0.43, and 0.40 $W\ m^{-1}\ K^{-1}$ at 300 K, respectively. The κ_{tot} of the control sample gradually decreases with increasing temperature up to 773 K, followed by a slight increase due to the *Pnma-Cmcm* phase transition[32] (Figure 7A). Note that the κ_{tot} of the title samples upturns at a considerably lower temperature of $\sim$573 K compared with $\sim$773 K observed for pristine SnSe,[38] attributed to Pb alloying.
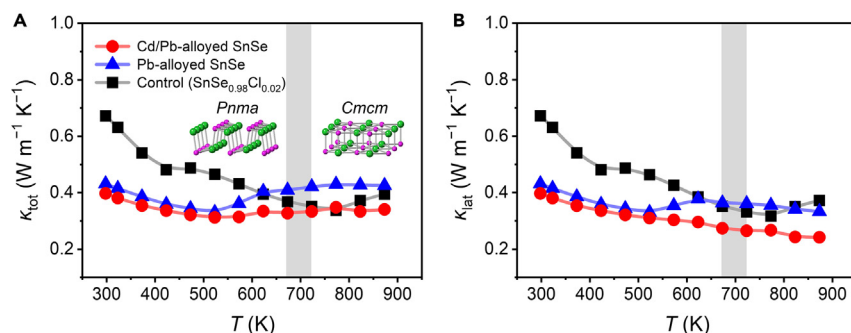
Figure 7. Thermal transport properties

Temperature-dependent (A) total (κ_{tot}) and (B) lattice thermal conductivity (κ_{lat}) parallel to the SPS pressing direction for the control, Pb-alloyed SnSe, and Cd/Pb-alloyed SnSe samples. The continuous *Pnma-Cmcm* phase transition region between 673 and 723 K for the Cd/Pb-alloyed SnSe sample is presented in gray.

After the upturn temperature, the κ_{tot} of the Pb-alloyed SnSe increases more steeply than that of the Cd/Pb-alloyed SnSe sample, reaching ~0.40 and ~0.33 W m^{-1} K^{-1} at 623 K, respectively, with similar values afterward. The κ_{tot} of the Cd/Pb-alloyed SnSe sample is ~0.34 W m^{-1} K^{-1} at 873 K in comparison with ~0.31 W m^{-1} K^{-1} at 798 K for $Sn_{0.97}Re_{0.03}Se_{0.93}Cl_{0.02}$[29]; ~0.36 W m^{-1} K^{-1} at 783 K for textured $Sn_{1.005}Se_{0.94}Br_{0.06}$[30]; ~0.39 W m^{-1} K^{-1} at 793 K for $Sn_{1.08}Se_{0.97}Br_{0.03}$−13% PbTe[31]; and ~0.35 W m^{-1} K^{-1} at 798 K for $SnSe_{0.92}$ + 1% $MoCl_5$.[32]

As κ_{tot} comprises contributions from both charge carriers (κ_{ele}) and lattice phonons (κ_{lat}), subtracting κ_{ele} (Figure S11) from κ_{tot} using the Wiedeman-Franz relationship (details in supplemental information) reveals the impact of Cd/Pb alloying on thermal transport (Figure 7B). The Pb-alloyed SnSe and Cd/Pb-alloyed SnSe samples exhibit significantly lower κ_{lat} values than the control sample at lower temperatures, which is ascribed to improved phonon scattering by the heavier Pb point defects, as directly observed in our STEM results.[42,48] Notably, the κ_{lat} of the title samples continuously decreases even above the T_c, in contrast to typical polycrystalline n-type SnSe materials. The κ_{lat} of the Pb-alloyed SnSe sample upturns at 573 K and outpaces that of the control sample above 673 K. This phenomenon is not attributed to bipolar effect, as |S| continuously increases with temperature, indicating no thermal activation of minority carriers. Such an upturn of κ_{lat} in the intermediate- to high-temperature regime has been frequently observed in SnSe,[38,49] for example, SnSe−y% PbTe.[31]

Remarkably, Cd alloying proves highly effective in suppressing κ_{lat}, especially above 523 K, resulting in a gradual decrease without an upturn trend. This observation underscores the significance of employing multiple strategies to further reduce κ_{lat} of SnSe, despite its already ultralow baseline. The diminished κ_{lat} can be attributed to the defect structure induced by the displaced Cd atom from the ideal cation sublattice. Similar reductions in κ_{lat} in such a temperature region have been observed with the introduction of nanoscale precipitates in materials such as $Sn_{1+x}Se$−y% $PbTe$[31] and $Sn_{0.99}Na_{0.01}Se$−Ag_8SnSe_6.[49] The lowest κ_{lat} value of the Cd/Pb-alloyed SnSe sample is ~0.24 W m^{-1} K^{-1} at 873 K. In comparison, the n-type polycrystalline $SnSe_{0.92}$ + 1% $MoCl_5$[32] shows ~0.30 W m^{-1} K^{-1} at 798 K parallel to the SPS pressing direction, and the n-type single-crystal SnSe ~0.20 W m^{-1} K^{-1} at 773 K along the out-of-plane direction.[20]
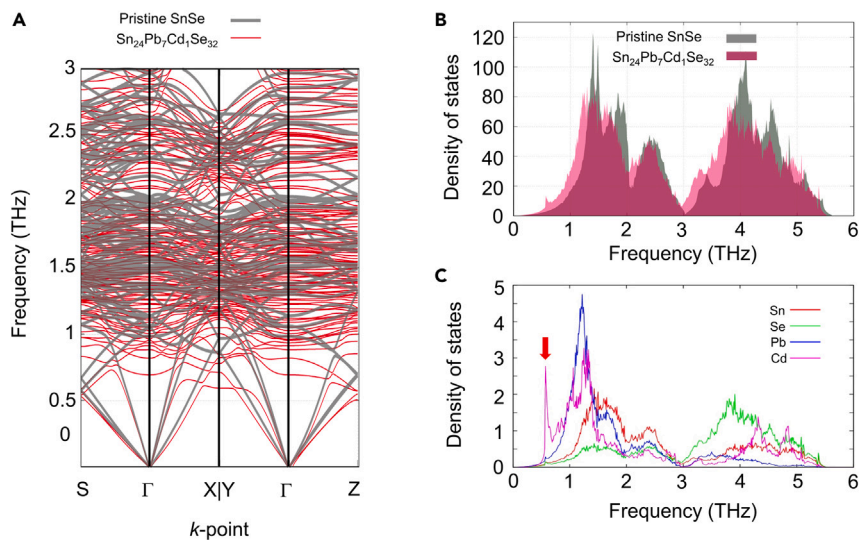
Figure 8. Phonon band structures

(A and B) (A) Phonon band structures and (B) density of states (DOS) of pristine and Cd/Pb-alloyed configuration of $Sn_{24}Pb_7Cd_1Se_{32}$.

(C) Atom-projected DOS of phonon structures of $Sn_{24}Pb_7Cd_1Se_{32}$.

Phonon band structures

The theoretical analysis of phonon band structure for the title configuration $Cd_1Sn_{24}Pb_7Se_{32}$ clearly reveals the role of the alloyed Pb and Cd atoms in achieving ultralow κ_{lat} (Figures 8A and 8B). The results show significantly softened phonon bands compared with those of pristine SnSe. High concentration Pb alloying induces mass fluctuations that soften both acoustic and optical phonon modes. The projected phonon DOS diagram clearly elucidates the ultralow κ_{lat} exhibited by the title samples. Notably, the Pb atom makes a substantial contribution to the lower frequency phonon regions of 0.5–1.5 THz, whereas the Sn and Se atoms contribute to the 1–3 and 3–5 THz ranges, respectively. Remarkably, the Cd alloying induces a distinctive localized band, marked by the red arrow, which crosses the acoustic phonon modes (Figure 8C). This unique feature has the potential to further suppress κ_{lat} through resonant scattering,[50] as confirmed by our experimental observations.

Figure of merit

Note that all samples show a maximum ZT (ZT_{max}) in their *Cmcm* phase. The Cd/Pb-alloyed SnSe sample exhibits a higher ZT over the entire temperature range than the others (Figure 9A). Its ZT_{max} is ~2.23 at 873 K in comparison with ~1.70 at 873 K for the Pb-alloyed SnSe and ~0.62 at 823 K for the control sample. It shows a ZT_{max} of ~0.95 at 873 K perpendicular to the SPS direction, indicating highly anisotropic TE performance of layered SnSe (Figure S12). The achieved ZT_{max} stands out as the highest among all n-type polycrystalline SnSe-based TE materials (Figure 9B), outperforming any other polycrystalline n-type TE materials, including n-type PbTe-based systems. Examples of representative polycrystalline n-type TE systems, along with their best-performing composition and ZT_{max} values, include $AgPb_mSbTe_{2+m}$ (~2.2 for $AgPb_{18}SbTe_{20}$)[14]; PbSe (~1.8 for $PbSe_{0.998}Br_{0.002}-2\% Cu_2Se$)[8]; PbTe (~1.9 for $Pb_{0.98}Sb_{0.02}Te$)[37]; skutterudite (~1.7 for $Ba_{0.08}La_{0.05}Yb_{0.04}Co_4Sb_{12}$)[51]; and half-Heusler alloys (~1.4 for $(Hf_{0.6}Zr_{0.4})NiSn_{0.99}Sb_{0.01}$).[52]

Three independently synthesized Cd/Pb-alloyed SnSe samples exhibit consistent σ, S, κ_{tot}, and ZT values within the instrumental errors, confirming the highly
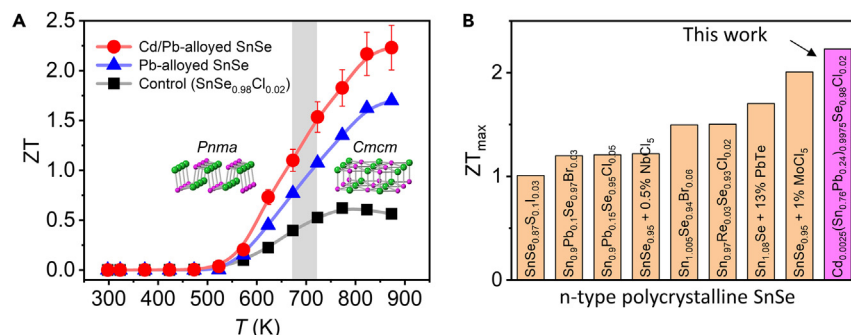
Figure 9. Thermoelectric figure of merit (ZT) values

(A) The temperature-dependent ZT value parallel to the SPS pressing direction for the control, Pb-alloyed SnSe, and Cd/Pb-alloyed SnSe samples. The title samples exhibit a maximum ZT (ZT_{max}) value after the phase transition. The continuous $Pnma$-$Cmcm$ phase transition region between 673 and 723 K for the Cd/Pb-alloyed SnSe sample is presented in gray. The error bar indicates a typical uncertainty of 10% for ZT estimation.

(B) A comparison of ZT_{max} of the Cd/Pb-alloyed SnSe sample with the other top-performing n-type polycrystalline SnSe materials.[29–35,61]

reproducible TE performances of the title system (Figure S13). They do not deteriorate throughout repetitive heating and cooling cycles according to the powder XRD patterns before and after TE property measurements (Figure S8). These features are of supreme importance in practical applications of TE technology.

Conclusions

We demonstrated that the incorporation of both Pb and Cd atoms plays a pivotal role in manipulating the electronic and phonon band structures of SnSe, resulting in extraordinarily high n-type TE performance. This innovative engineering targets the conduction bands of both the $Pnma$ and $Cmcm$ phases, enhancing the DOS near the Fermi level through the convergence and flattening of conduction band minima, coupled with the increased DOS effective mass. Consequently, the magnitude of Seebeck coefficients sees a significant increase without compromising electrical conductivity. Notably, despite the elevated DOS effective mass and Seebeck coefficients, charge carrier mobility is only modestly affected. This can be attributed to the exclusively divalent Pb and Cd cations filling intrinsically evolving Sn vacancies.

Much heavier Pb and displaced Cd atoms prove effective in substantially softening and scattering heat-carrying phonons, thereby suppressing thermal conductivity. Particularly, the alloyed Cd, even at trace-level concentrations, continuously depresses lattice thermal conductivity from 300 to 873 K, spanning the phase transition region of 673–723 K. As a result, the title compound exhibits a remarkable ZT_{max} of ~2.23 at 873 K, representing the highest reported value to date for all n-type polycrystalline TE systems, including PbTe-based materials.

This achievement underscores the importance of discovering new compositions and employing innovative strategies to enhance TE performance. Notably, the synthesized title system is readily achievable through traditional solid-state reaction methods, eliminating the need for complicated synthesis and production processes. This simplicity makes it highly suitable for reliable and reproducible mass production. The exceedingly high ZT of our n-type polycrystalline SnSe materials holds great promise for practical applications, offering economically viable and ultra-high-performance SnSe thermoelectrics.

EXPERIMENTAL PROCEDURES

Resource availability

Lead contact

Further information and requests for resources and materials should be directed to and will be fulfilled by the lead contact, In Chung (inchung@snu.ac.kr).

Materials availability

New materials generated in this study are available from the lead contact upon reasonable request with a completed materials transfer agreement.

Data and code availability

All datasets utilized in this study are available within the article and are described in the supplemental information or are available from the corresponding author upon reasonable request. There was no code generated in this study.

Reagents

The starting reagents were used as received unless specified otherwise except for Sn:Sn chunk (99.999% American Elements, USA), Se shot (99.999%, 5N Plus, Canada), Pb wire (99.99%, 5N Plus, Canada), anhydrous $SnCl_2$ powder (99.99%, Sigma-Aldrich), and Cd powder (99.99%, Alfa Aesar, USA). Note that as-received elemental Sn chunks were purified to eliminate tin oxides possibly present. They were loaded into an evacuated fused-silica tube at 10^{-4} Torr. The tube was heated at 623 K for 3 h, followed by cooling to room temperature. The resulting Sn ingot contained ash-like black residues at its top and surface. They were physically removed. The same melting-purification process was repeated three times until the black residues were no longer observed.

Synthesis

All syntheses and sample preparations were conducted in a 99.999% purity Ar-filled glovebox with the level of moisture and oxygen at 0 and less than 1 ppm, respectively. To synthesize title and control samples, a proper ratio of starting reagents was loaded to an evacuated fused-silica tube with an internal pressure of $\sim 10^{-4}$ Torr. The total weight of reactants was approximately 13 g. The reaction tubes were inserted to a larger evacuated fused-silica tube to protect reaction products from oxidation in the case of cracks of the inner tube during a cooling process. The resulting double-sealed tubes were heated to 1,223 K in 9 h, soaked for 12 h, and rapidly quenched to cold water. The obtained ingots were ground into fine powders by a mechanical grinder, and loaded into a graphite die. They were densified at $\sim$783 K for 5 min under an axial pressure of 50 MPa in a vacuum of $\sim 1.4 \times 10^{-2}$ Torr utilizing a SPS instrument (SPS-211Lx, Fuji Electronic Industrial, Japan).

Electrical and thermal transport property measurements

The SPS-processed samples were cut and polished into various shapes and dimensions. The Seebeck coefficient and electrical conductivity were concurrently measured using bar-shaped samples with dimensions of $\sim$12 × 3 × 3 mm^3 on an ULVAC-RIKO ZEM-3 instrument under a low-pressure He atmosphere from room temperature to 823 K. Hall effect measurements were taken using a Lakeshore 8407 system from 300 to 873 K under an ultrahigh vacuum ($<10^{-5}$ Pa) with a reversible 1.5 T magnetic field and 1 mA excitation current. The thermal diffusivity (D) of the samples coated with graphite was measured on a Netzsch LFA 457 MicroFlash instrument (Figure S14). The thermal conductivity was calculated by the relation $\kappa_{tot} = \rho \cdot D \cdot C_p$, where ρ is the mass density of the specimens, D is the measured thermal diffusivity, and C_p is the heat capacity. The ρ values used were obtained by their

geometrical dimensions and masses. The specific heat capacity C_P per atom throughout the temperature range 300–873 K was determined using the Dulong-Petit law $C_P = 3k_B$. The κ_{tot} is a sum of the lattice (κ_{lat}) and electronic thermal (κ_{ele}) conductivities. κ_{ele} is proportional to the electrical conductivity (σ) according to the Wiedemann-Franz relation ($\kappa_{ele} = L \cdot \sigma \cdot T$), where L is the temperature-dependent Lorenz number and T is the absolute temperature. An L value as a function of temperature was obtained from a SPB model (see supplemental information for the details). The κ_{lat} value was taken by the relation of $\kappa_{lat} = \kappa_{tot} - \kappa_{ele}$.

Scanning transmission electron microscopy

Specimens for cross-sectional STEM were fabricated by focused ion beams (FIBs, Helios 650, FEI) employing a dual-beam microscope with gallium ion milling. Before an ion milling process, the surface of specimens was coated with carbon by sputtering for protection. Microstructures and chemical compositions were analyzed by a spherical aberration-corrected JEM ARM-200F microscope (cold field emission gun [FEG] type, Jeol) equipped with a silicon drift detector (SDD) type EDS detector (solid angle 0.9-sr, X-MaxN 100TLE, Oxford) and EELS detector (965 GIF Quantum ER, Gatan) at 200 kV installed at the National Center for Inter-university Research Facilities (NCIRF) in Seoul National University. In HAADF-STEM images, the point-to-point resolution was approximately 80 pm after the application of the spherical aberration correction and the angular range of the annular detector used was from 68 to 280 mrad. All STEM images were obtained using a high-resolution CCD detector with a 2,000 × 2,000 pixel device in the GIF-QuantumER imaging filter (Gatan). Elemental scanning maps by STEM-EDS were recorded with a probe size of 0.13 nm and a probe current of 40 pA.

DFT calculations

For all calculations, we utilized a plane-wave basis set with a cut-off energy of 350 eV and the projector augmented wave method[53] that is implemented in the Vienna *Ab initio* Simulation Package.[54,55] We optimized structures and calculated electronic and phonon band structures of the title and control samples within the DFT formalism. We employed the HSE06 hybrid functionals[56] and the van der Waals interaction within the Tkatchenko and Scheffler formalism[57] for lattice optimizations, and the SCAN+rVV10 meta-generalized gradient approximation (meta-GGA) functional[58] for further relaxations of internal coordinates. Accordingly, we could obtain lattice parameters best agreeing with experimental results and optimized internal coordinates that are well-matched with further calculations of electronic structures. In order to avoid unnecessary phase change between high- and low-temperature phases, we employed a quasi-Newton algorithm for ionic relaxation. To calculate electronic structures, we also utilized the SCAN+rVV10 meta-GGA functional.[58] For the momentum space sampling, we used 3 × 3 × 3 for the hybrid functional with the downsampling of k-point scheme[58] and 4 × 4 × 4 for the meta-GGA functional. All structures were relaxed until the atomic force reached less than 0.01 eV Å^{-1}. We utilized a $2\sqrt{2} \times 2\sqrt{2} \times 1$ supercells accommodating 64 atoms at the lattice points to calculate the *Pnma* and *Cmcm* phases. We employed the Perdew-Burke-Ernzerhof adapted for solids (PBEsol) functional[59] for phonon band structures to obtain force constants and utilized the phonopy code[60] to calculate the phonon band structure of the title and control samples.

SUPPLEMENTAL INFORMATION

Supplemental information can be found online at https://doi.org/10.1016/j.joule.2024.02.013.

Joule
Article

REFERENCES

1. The 2022 Energy Flow Charts: Charting the Complex Relationships among Energy, Water, and Carbon (Lawrence Livermore National Laboratory). https://flowcharts.llnl.gov/.

2. Jood, P., Ohta, M., Yamamoto, A., and Kanatzidis, M.G. (2018). Excessively doped PbTe with Ge-induced nanostructures enables high-efficiency thermoelectric modules. Joule 2, 1339–1355.

3. Park, S.H., Jin, Y., Cha, J., Hong, K., Kim, Y., Yoon, H., Yoo, C.-Y., and Chung, I. (2018). High-power-density skutterudite-based thermoelectric modules with ultralow contact resistivity using Fe−Ni metallization layers. ACS Appl. Energy Mater. 1, 1603–1611.

4. Tan, G., Zhao, L.-D., and Kanatzidis, M.G. (2016). Rationally designing high-performance bulk thermoelectric materials. Chem. Rev. 116, 12123–12149.

5. Kanatzidis, M.G. (2010). Nanostructured thermoelectrics: the new paradigm? Chem. Mater. 22, 648–659.

6. Hodges, J.M., Hao, S., Grovogui, J.A., Zhang, X., Bailey, T.P., Li, X., Gan, Z., Hu, Y.-Y., Uher, C., Dravid, V.P., et al. (2018). Chemical insights into PbSe−x% HgSe: high power factor and improved thermoelectric performance by alloying with discordant atoms. J. Am. Chem. Soc. 140, 18115–18123.

7. Zhou, C., Lee, Y.K., Cha, J., Yoo, B., Cho, S.-P., Hyeon, T., and Chung, I. (2018). Defect engineering for high-performance n-type PbSe thermoelectrics. J. Am. Chem. Soc. 140, 9282–9290.

8. Zhou, C., Yu, Y., Lee, Y.K., Cojocaru-Mirédin, O., Yoo, B., Cho, S.-P., Im, J., Wuttig, M., Hyeon, T., and Chung, I. (2018). High-performance n-type PbSe−Cu2Se thermoelectrics through conduction band engineering and phonon softening. J. Am. Chem. Soc. 140, 15535–15545.

9. Zhou, C., Yu, Y., Lee, Y.-L., Ge, B., Lu, W., Cojocaru-Mirédin, O., Im, J., Cho, S.-P., Wuttig, M., Shi, Z., et al. (2020). Exceptionally high average power factor and thermoelectric figure of merit in n-type PbSe by the dual incorporation of Cu and Te. J. Am. Chem. Soc. 142, 15172–15186.

10. Zhou, C., and Chung, I. (2020). Nanoscale defect structures advancing high performance n-type PbSe thermoelectrics. Coord. Chem. Rev. 421, 213437.

11. Ge, B., Lee, H., Im, J., Choi, Y., Kim, S.-Y., Lee, J.Y., Cho, S.-P., Sung, Y.-E., Choi, K.-Y., Zhou, C., et al. (2023). Engineering an atomic-level crystal lattice and electronic band structure for extraordinarily high average thermoelectric figure of merit in n-type PbSe. Energy Environ. Sci. 16, 3994–4008.

12. Zhou, C., Yu, Y., Zhang, X., Cheng, Y., Xu, J., Lee, Y.K., Yoo, B., Cojocaru-Mirédin, O., Liu, G., Cho, S.P., et al. (2020). Cu intercalation and Br doping to thermoelectric SnSe2 lead to ultrahigh electron mobility and temperature-independent power factor. Adv. Funct. Mater. 30, 1908405.

13. Ge, B., Lee, H., Huang, L., Zhou, C., Wei, Z., Cai, B., Cho, S.P., Li, J.F., Qiao, G., Qin, X., et al. (2022). Atomic level defect structure engineering for unusually high average thermoelectric figure of merit in n-type PbSe rivalling PbTe. Adv. Sci. 9, e2203782.

14. Hsu, K.F., Loo, S., Guo, F., Chen, W., Dyck, J.S., Uher, C., Hogan, T., Polychroniadis, E.K., and Kanatzidis, M.G. (2004). Cubic AgPbmSbTe2+m: bulk thermoelectric materials with high figure of merit. Science 303, 818–821.

15. Biswas, K., He, J., Zhang, Q., Wang, G., Uher, C., Dravid, V.P., and Kanatzidis, M.G. (2011). Strained endotaxial nanostructures with high thermoelectric figure of merit. Nat. Chem. 3, 160–166.

16. Biswas, K., He, J., Blum, I.D., Wu, C.-I., Hogan, T.P., Seidman, D.N., Dravid, V.P., and Kanatzidis, M.G. (2012). High-performance bulk thermoelectrics with all-scale hierarchical architectures. Nature 489, 414–418.

17. Tan, G., Shi, F., Hao, S., Zhao, L.-D., Chi, H., Zhang, X., Uher, C., Wolverton, C., Dravid, V.P., and Kanatzidis, M.G. (2016). Non-equilibrium processing leads to record high thermoelectric figure of merit in PbTe−SrTe. Nat. Commun. 7, 12167.

18. Jiang, B., Yu, Y., Cui, J., Liu, X., Xie, L., Liao, J., Zhang, Q., Huang, Y., Ning, S., Jia, B., et al. (2021). High-entropy-stabilized chalcogenides with high thermoelectric performance. Science 371, 830–834.

19. Zhao, L.-D., Lo, S.-H., Zhang, Y., Sun, H., Tan, G., Uher, C., Wolverton, C., Dravid, V.P., and Kanatzidis, M.G. (2014). Ultralow thermal conductivity and high thermoelectric figure of merit in SnSe crystals. Nature 508, 373–377.

20. Chang, C., Wu, M., He, D., Pei, Y., Wu, C.-F., Wu, X., Yu, H., Zhu, F., Wang, K., Chen, Y., et al. (2018). 3D charge and 2D phonon transports leading to high out-of-plane ZT in n-type SnSe crystals. Science 360, 778–783.

21. Lee, Y.K., Luo, Z., Cho, S.P., Kanatzidis, M.G., and Chung, I. (2019). Surface oxide removal for polycrystalline SnSe reveals near-single-crystal thermoelectric performance. Joule 3, 719–731.

22. Zhou, C., Lee, Y.K., Yu, Y., Byun, S., Luo, Z.-Z., Lee, H., Ge, B., Lee, Y.-L., Chen, X., Lee, J.Y., et al. (2021). Polycrystalline SnSe with a thermoelectric figure of merit greater than the single crystal. Nat. Mater. 20, 1378–1384.

23. Liu, D., Wang, D., Hong, T., Wang, Z., Wang, Y., Qin, Y., Su, L., Yang, T., Gao, X., Ge, Z., et al.

(2023). Lattice plainification advances highly effective SnSe crystalline thermoelectrics. Science 380, 841–846.

24. Chung, I. (2023). Plainly fixing crystal lattices. Science 380, 800.

25. Munirathnappa, A.K., Lee, H., and Chung, I. (2023). Recent advances in ultrahigh thermoelectric performance material SnSe. Mater. Lab. 2, 220056.

26. Kim, T., Lee, H., and Chung, I. (2024). SnSe: the rise of the ultrahigh thermoelectric performance material. Bull. Korean Chem. Soc. https://doi.org/10.1002/bkcs.12821.

27. Wei, P.-C., Bhattacharya, S., He, J., Neeleshwar, S., Podila, R., Chen, Y.Y., and Rao, A.M. (2016). The intrinsic thermal conductivity of SnSe. Nature 539, E1–E2.

28. Zhao, L.D., Lo, S.H., Zhang, Y., Sun, H., Tan, G., Uher, C., Wolverton, C., Dravid, V.P., and Kanatzidis, M.G. (2016). Zhao et al. reply. Nature 539, E2–E3.

29. Ge, Z.H., Qiu, Y., Chen, Y.X., Chong, X., Feng, J., Liu, Z.K., and He, J. (2019). Multipoint defect synergy realizing the excellent thermoelectric performance of n-type polycrystalline SnSe via Re doping. Adv. Funct. Mater. 29, 1902893.

30. Shang, P.-P., Dong, J., Pei, J., Sun, F.-H., Pan, Y., Tang, H., Zhang, B.-P., Zhao, L.-D., and Li, J.-F. (2019). Highly textured n-type SnSe polycrystals with enhanced thermoelectric performance. Research 2019, 9253132.

31. Su, L., Hong, T., Wang, D., Wang, S., Qin, B., Zhang, M., Gao, X., Chang, C., and Zhao, L.-D. (2021). Realizing high doping efficiency and thermoelectric performance in n-type SnSe polycrystals via bandgap engineering and vacancy compensation. Mater. Today Phys. 20, 100452.

32. Chandra, S., Bhat, U., Dutta, P., Bhardwaj, A., Datta, R., and Biswas, K. (2022). Modular nanostructures facilitate low thermal conductivity and ultra-high thermoelectric performance in n-type SnSe. Adv. Mater. 34, e2203725.

33. Cha, J., Zhou, C., Lee, Y.K., Cho, S.-P., and Chung, I. (2019). High thermoelectric performance in n-type polycrystalline SnSe via dual incorporation of Cl and PbSe and dense nanostructures. ACS Appl. Mater. Interfaces 11, 21645–21654.

34. Zhang, Q., Chere, E.K., Sun, J., Cao, F., Dahal, K., Chen, S., Chen, G., and Ren, Z. (2015). Studies on thermoelectric properties of n-type polycrystalline $SnSe_{1−x}S_x$ by iodine doping. Adv. Energy Mater. 5, 1500360.

35. Chang, C., Tan, Q., Pei, Y., Xiao, Y., Zhang, X., Chen, Y.-X., Zheng, L., Gong, S., Li, J.-F., He, J., et al. (2016). Raising thermoelectric performance of n-type SnSe via Br doping and Pb alloying. RSC Adv. 6, 98216–98220.

36. Qin, B., Wang, D., Liu, X., Qin, Y., Dong, J.-F., Luo, J., Li, J.-W., Liu, W., Tan, G., Tang, X., et al. (2021). Power generation and thermoelectric cooling enabled by momentum and energy multiband alignments. Science 373, 556–561.

37. Xu, P., Zhao, W., Liu, X., Jia, B., He, J., Fu, L., and Xu, B. (2022). Dramatic enhancement of

thermoelectric performance in PbTe by unconventional grain shrinking in the sintering process. Adv. Mater. 34, e2202949.

38. Lee, Y.K., Ahn, K., Cha, J., Zhou, C., Kim, H.S., Choi, G., Chae, S.I., Park, J.-H., Cho, S.-P., Park, S.H., et al. (2017). Enhancing p-type thermoelectric performances of polycrystalline SnSe via tuning phase transition temperature. J. Am. Chem. Soc. 139, 10887–10896.

39. Wu, P., Ishikawa, Y., Hagihala, M., Lee, S., Peng, K., Wang, G., Torii, S., and Kamiyama, T. (2018). Crystal structure of high-performance thermoelectric materials by high resolution neutron powder diffraction. Physiol. 551, 64–68.

40. Gainza, J., Serrano-Sánchez, F., Gharsallah, M., Carrascoso, F., Bermúdez, J., Dura, O.J., Mompean, F.J., Biskup, N., Meléndez, J.J., Martínez, J.L., et al. (2019). Evidence of nanostructuring and reduced thermal conductivity in n-type Sb-alloyed SnSe thermoelectric polycrystals. J. Appl. Phys. 126, 045105.

41. Li, X., Chen, C., Xue, W., Li, S., Cao, F., Chen, Y., He, J., Sui, J., Liu, X., Wang, Y., et al. (2018). N-type Bi-doped SnSe thermoelectric nanomaterials synthesized by a facile solution method. Inorg. Chem. 57, 13800–13808.

42. Chang, C., Wang, D., He, D., He, W., Zhu, F., Wang, G., He, J., and Zhao, L.D. (2019). Realizing high-ranged out-of-plane ZTs in n-type SnSe crystals through promoting continuous phase transition. Adv. Energy Mater. 9, 1901334.

43. Luo, Z.-Z., Hao, S., Zhang, X., Hua, X., Cai, S., Tan, G., Bailey, T.P., Ma, R., Uher, C., Wolverton, C., et al. (2018). Soft phonon modes from off-center Ge atoms lead to ultralow thermal conductivity and superior thermoelectric performance in n-type PbSe−GeSe. Energy Environ. Sci. 11, 3220–3230.

44. Cai, S., Hao, S., Luo, Z.-Z., Li, X., Hadar, I., Bailey, T.P., Hu, X., Uher, C., Hu, Y.-Y., Wolverton, C., et al. (2020). Discordant nature of Cd in PbSe: off-centering and core−shell nanoscale CdSe precipitates lead to high thermoelectric performance. Energy Environ. Sci. 13, 200–211.

45. Shi, X., Wu, A., Feng, T., Zheng, K., Liu, W., Sun, Q., Hong, M., Pantelides, S.T., Chen, Z.-G., and Zou, J. (2019). High thermoelectric performance in p-type polycrystalline Cd-doped SnSe achieved by a combination of cation vacancies and localized lattice engineering. Adv. Energy Mater. 9, 1803242.

46. Feser, J.P., Chan, E.M., Majumdar, A., Segalman, R.A., and Urban, J.J. (2013). Ultralow thermal conductivity in polycrystalline CdSe thin films with controlled grain size. Nano Lett. 13, 2122–2127.

47. Wei, T.-R., Tan, G., Zhang, X., Wu, C.-F., Li, J.-F., Dravid, V.P., Snyder, G.J., and Kanatzidis, M.G. (2016). Distinct impact of alkali-ion doping on electrical transport properties of thermoelectric p-type polycrystalline SnSe. J. Am. Chem. Soc. 138, 8875–8882.

48. Kim, H.S., Choi, G., Ha, M.Y., Kim, D.H., Park, S.H., Chung, I., and Lee, W.B. (2019). Thermoelectric transport properties of Pb

doped SnSe alloys ($Pb_xSn_{1−x}Se$): DFT-BTE simulations. J. Solid State Chem. 270, 413–418.

49. Luo, Y., Cai, S., Hua, X., Chen, H., Liang, Q., Du, C., Zheng, Y., Shen, J., Xu, J., Wolverton, C., et al. (2019). High thermoelectric performance in polycrystalline SnSe via dual-doping with Ag/Na and nanostructuring with Ag_8SnSe_6. Adv. Energy Mater. 9, 1803072.

50. Tse, J.S., Li, Z., and Uehara, K. (2001). Phonon band structures and resonant scattering in Na_8Si_{46} and Cs_8Sn_{44} clathrates. Europhys. Lett. 56, 261–267.

51. Shi, X., Yang, J., Salvador, J.R., Chi, M., Cho, J.Y., Wang, H., Bai, S., Yang, J., Zhang, W., and Chen, L. (2011). Multiple-filled skutterudites: high thermoelectric figure of merit through separately optimizing electrical and thermal transports. J. Am. Chem. Soc. 133, 7837–7846.

52. Kang, H.B., Poudel, B., Li, W., Lee, H., Saparamadu, U., Nozariasbmarz, A., Kang, M.G., Gupta, A., Heremans, J.J., and Priya, S. (2020). Decoupled phononic-electronic transport in multi-phase n-type half-Heusler nanocomposites enabling efficient high temperature power generation. Mater. Today 36, 63–72.

53. Blöchl, P.E. (1994). Projector augmented-wave method. Phys. Rev. B Condens. Matter 50, 17953–17979.

54. Kresse, G., and Hafner, J. (1994). Norm-conserving and ultrasoft pseudopotentials for first-row and transition elements. J. Phys.: Condens. Matter 6, 8245–8257.

55. Kresse, G., and Furthmüller, J. (1996). Efficient iterative schemes for ab initio total-energy calculations using a plane-wave basis set. Phys. Rev. B Condens. Matter 54, 11169–11186.

56. Krukau, A.V., Vydrov, O.A., Izmaylov, A.F., and Scuseria, G.E. (2006). Influence of the exchange screening parameter on the performance of screened hybrid functionals. J. Chem. Phys. 125, 224106.

57. Tkatchenko, A., and Scheffler, M. (2009). Accurate molecular van der Waals interactions from ground-state electron density and free-atom reference data. Phys. Rev. Lett. 102, 073005.

58. Paier, J., Marsman, M., Hummer, K., Kresse, G., Gerber, I.C., and Ángyán, J.G. (2006). Screened hybrid density functionals applied to solids. J. Chem. Phys. 124, 154709.

59. Perdew, J.P., Ruzsinszky, A., Csonka, G.I., Vydrov, O.A., Scuseria, G.E., Constantin, L.A., Zhou, X., and Burke, K. (2008). Restoring the density-gradient expansion for exchange in solids and surfaces. Phys. Rev. Lett. 100, 136406.

60. Togo, A., Chaput, L., Tadano, T., and Tanaka, I. (2023). Implementation strategies in phonopy and phono3py. J. Phys. Condens. Matter 35, 353001.

61. Cai, J., Zhang, Y., Yin, Y., Tan, X., Duan, S., Liu, G.-Q., Hu, H., Xiao, Y., Ge, Z., and Jiang, J. (2020). Investigating the thermoelectric performance of n-type SnSe: the synergistic effect of $NbCl_5$ doping and dislocation engineering. J. Mater. Chem. C 8, 13244–13252.